ACS APPLIED MATERIALS & INTERFACES

Research Article

Cite This: ACS Appl. Mater. Interfaces 2018, 10, 44614−44623

www.acsami.org

Friction and Adhesion of Different Structural Defects of Graphene

Manoj Tripathi,[†] Firas Awaja,[‡] Rafael A. Bizao,[§] Stefano Signetti,[∥] Erica Iacob,[⊥] Guido Paolicelli,[#] Sergio Valeri,[#,∇] Alan Dalton,[†] and Nicola Maria Pugno*[,§,○,◆]

[†]Department of Mathematics and Physical Sciences, University of Sussex, Brighton BN1 9RH, United Kingdom

[‡]Department of Orthopaedic Surgery, Medical University Innsbruck, Innrain 36, Innsbruck, Austria

[§]Laboratory of Bio-Inspired & Graphene Nanomechanics, Department of Civil, Environmental and Mechanical Engineering, University of Trento, via Mesiano 77 I-38123 Trento, Italy

[∥]Department of Mechanical Engineering, Korea Advanced institute of Science and Technology (KAIST), 291 Daehak-ro, Yuseong-gu, Daejeon 34141, Republic of Korea

[⊥]Centre for Materials and Microsystems, Fondazione Bruno Kessler, via Sommarive 18, I-38123 Trento, Italy

[#]Istituto Nanoscienze, Consiglio Nazionale delle Ricerche, via G. Campi 213/a, 41125- Modena, Italy

[∇]Dipartimento di Scienze Fisiche Informatiche e Matematiche (FIM), Università di Modena e Reggio Emilia, via Campi 213/a, I-41125 Modena, Italy

[○]School of Engineering and Materials Science, Queen Mary University of London, Mile End Road, E1 4NS London United Kingdom

[◆]Ket Lab, Edoardo Amaldi Foundation, via del Politecnico snc, I-00133 Roma, Italy

Supporting Information

ABSTRACT: Graphene structural defects, namely edges, step-edges, and wrinkles, are susceptible to severe mechanical deformation and stresses under tribo-mechanical operations. Applied forces may cause deformation by folding, buckling, bending, and tearing of these defective sites of graphene, which lead to a remarkable decline in normal and friction load bearing capacity. In this work, we experimentally quantified the maximum sustainable normal and friction forces, corresponding to the damage thresholds of the different investigated defects as well as their pull-out (adhesion) forces. Horizontal wrinkles (with respect to the basal plane, i.e., folded) sustained the highest normal load, up to 317 nN, during sliding, whereas for vertical (i.e., standing) wrinkles, step-edges, and edges, the load bearing capacities are up to 113, 74, and 63 nN, respectively. The related deformation mechanisms were also experimentally investigated by varying the normal load up to the initiation of the damage from the defects and extended with the numerical results from molecular dynamics and finite element method simulations.

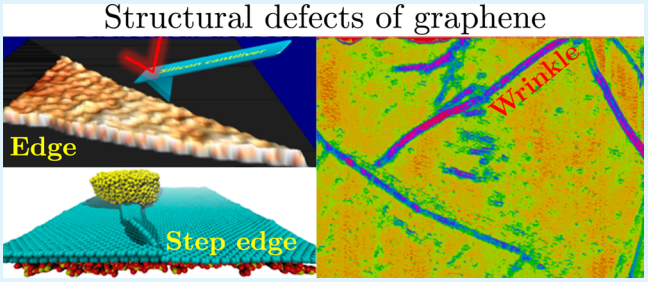

KEYWORDS: *AFM, graphene, defects, friction, adhesion*

INTRODUCTION

Graphene is a robust choice for coating surfaces to achieve improved tribological properties such as superlubricity,[1] tuned friction,[2] and high load bearing capability which results in antiwear characteristics.[3] Graphene failure under frictional loads[4−7] becomes predominant in the presence of structural defects, which are thus taking a central interest in the materials research community due to their implication on the advanced applications of graphene related materials. Most of the reported exotic characteristics of graphene refer to defect-free films thus neglecting the dramatic role of structural flaws and imperfections. The most recurrent structural defects are edges (E, i.e., the perimeter of an atomic layer over a different substrate), step-edges (SE, i.e., the perimeter of an atomic layer over another atomic layer), wrinkles (Wr),[8,9] grain boundaries (GB),[10,11] and vacancies.[12] These defects introduce significant alterations in the graphene properties that often compromise its durability and functionality. Grain boundaries and wrinkles, for example, can severely weaken the mechanical strength of graphene membranes. Indeed, the fracture strength might be decreased by orders of magnitude.[10,13] Isolated defects, such as monovacancies and Stone−Wales dislocations, slits, and holes also compromise the mechanical properties of graphene.[12,14−16]

E and SE are potentially the most dire defects among lamellar materials. Several reports explained that atoms

Received: September 6, 2018
Accepted: November 15, 2018
Published: November 15, 2018

DOI: 10.1021/acsami.8b10294
ACS Appl. Mater. Interfaces 2018, 10, 44614−44623

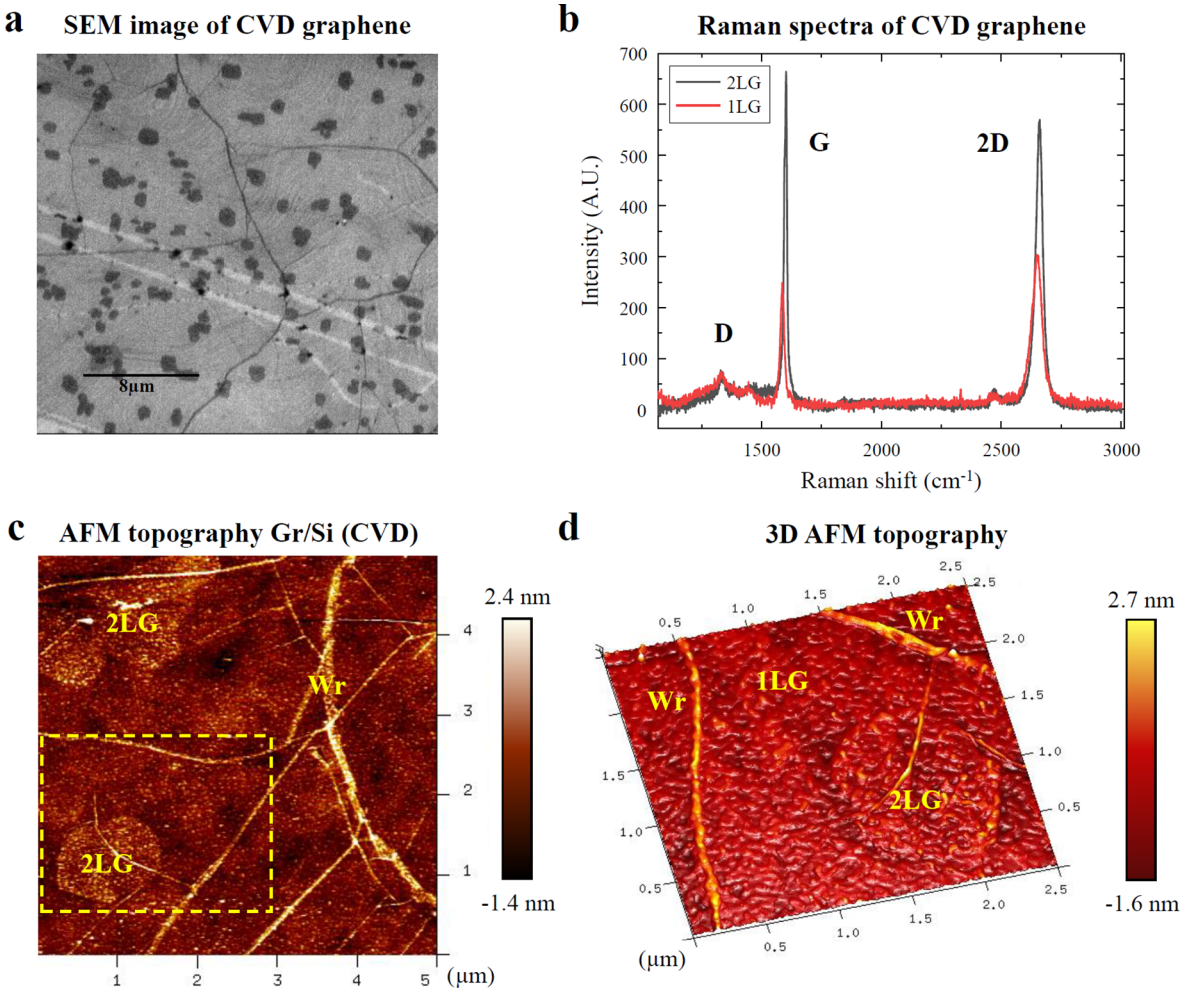

Figure 1. Topographical information of CVD graphene on silica substrate. (a) SEM image of the CVD graphene showing distribution of Wrs (dark lines) and 2LG (dark patches). (b) Raman spectra confirming the presence of 2LG and 1LG (from ratio of 2D and G peaks) with structural disorder (D-peak). (c) AFM topographical image showing the basal plane consisting of 1LG, some 2LG islands, and the network of crossing Wrs. (d) High-resolution 3D AFM topography showing morphological contrast between Wr and graphene basal plane.

belonging to E/SE behave differently from the atoms of basal plane in both physical[14,17,18] and chemical aspects[11,19] due to the presence of dangling bonds. Atomic force microscopy (AFM) studies revealed that the mechanical response of the E/SE defects is also strongly influenced by the size and shape of the AFM tip, environmental conditions (such as the presence of airborne impurities, nitrogen atmosphere, and vacuum), and surface energy landscape, as reported extensively.[20−25] For example, large energy barriers, i.e., the difference between maximum potential energy of slide probe at basal plane and at SE, was proposed by Ye and Martini[26] as the primary cause of graphene rupture during AFM operations. Other structural defects include Wr and GB, which are commonly produced during chemical vapor deposition (CVD) of polycrystalline graphene.[9,27] These structural defects have higher binding energy towards foreign particles than basal graphene plane which may be responsible for higher friction forces.[27] Yu et al.[27] revealed enhanced sp^3 state and lower van der Waals stabilization of Wr as compared to graphene basal plane, which causes the Wr detachment from the substrate. Vasic et al.[19] found that the load bearing capacity of graphene (i.e., threshold of normal force to initiate wear) significantly drops, by nearly 1 order of magnitude, in the presence of wrinkles.

AFM is one of the most effective techniques to study nanostructural surfaces and defects.[28,29] In particular, its sensitivity is able to detect short-range interactions at the atomic level[30] and to manipulate structures at the nano[31] and atomic scale.[32] Friction force microscopy (FFM), a subcategory of AFM technique, allows the detection of friction forces from atomic to micro scale. Sliding of the tip along the fast scan axis in contact with the substrate generates a lateral force (F_L) on the apex, which causes the cantilever torsion around its longitudinal axis. Accordingly, graphene surface defects, like vacancies, adsorbed atoms and molecules produce a visible contrast in the lateral force image.[22] Higher friction forces at E/SE and Wr are attributed to the Schwoebel-Ehrlich barrier at atomic steps[23,33] and to the ratchet effect[34,35] respectively. Recently, friction and wear phenomena of the edge of graphene on silica substrate have been explained through buckling and lower interaction of the edge atoms with silica surface,[19] whereas the height of the E region was reported to be higher than graphene basal plane,[20] due to puckering effect, and it is responsible for the folding and tearing of graphene edges.

In the present work, we compared the load bearing capacity, friction and adhesion forces for different types of line defects of 2D materials, namely E, SE, and Wr (horizontal and vertical

DOI: 10.1021/acsami.8b10294
ACS Appl. Mater. Interfaces 2018, 10, 44614−44623

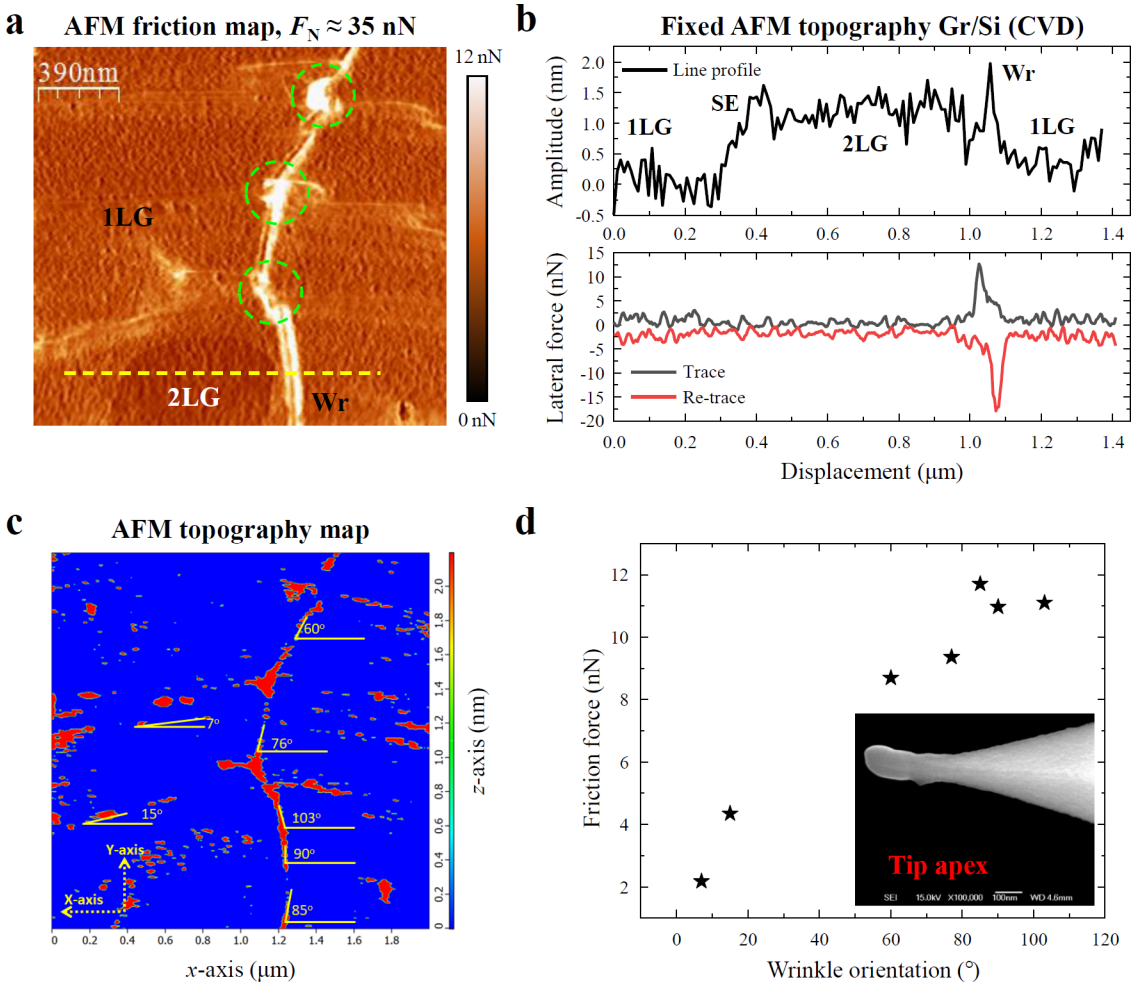

Figure 2. Friction force as a function of Wr orientation. (a) Friction map includes lateral force values measured in trace and retrace scanning direction of cantilever on CVD graphene, showing highest F_F on Wr, lowest on 2LG (bright color corresponds to higher friction force) and intermediate for 1LG. (b) Topography and lateral force line profile along 2LG region and at Wr (yellow dashed line on panel a). (c) Filtered topography image where Wrs have been highlighted as red regions with amplitude (height) above 2 nm. Their orientation is measured with respect to *x*-axis corresponding to fast scan direction. (d) Friction force as a function of Wr orientation at F_N = 35 nN. The inset SEM image shows the silicon tip used for the friction measurement.

types). In particular, we elucidated the frictional stability of structural defects for polycrystalline graphene. We also endeavored to comprehensively investigate the mechanical deformation phenomena of the E, SE, and Wr in graphene, conducted through the systematic increase of the applied normal force (F_N) and measuring the friction forces (F_F). Molecular dynamics (MD) and finite element method (FEM) simulations have been conducted in order to explicate the experimental observations.

RESULTS AND DISCUSSION

Commercially obtained CVD produced graphene transferred on silica substrate and mechanically exfoliated (ME) graphene have been used in our investigation. The scanning electron microscopy (SEM) image illustrating the distribution of single graphene layer (1LG, bright color), bilayer (2LG, dark patches) and Wrs is shown in Figure 1a. The presence of 1LG and 2LG is also verified via Raman spectroscopy by measuring the ratio intensity of 2D and G peaks[36] (Figure 1b). The AFM topography of graphene in Figure 1c shows various landscapes, namely 1LG, 2LG, SE, and Wr. The high-resolution 3D-AFM topography in Figure 1d shows a morphological contrast among the Wr and graphene basal plane of 1LG and 2LG. The distribution of Wrs and the intrinsic ripples in graphene significantly influence its roughness and topological conformation. The roughness (root-mean-square) of 1LG is measured as 0.320 nm, slightly higher than 2LG, which is 0.314 nm. The roughness of transferred CVD graphene is associated with the method of transfer, graphene thickness, substrate interaction, and tip radius used for the investigation.[37] In the present work, silicon cantilever tip (apex radius ~25 nm) is used for the roughness measurement and for the low load friction measurement (see Figure S1 in the Supporting Information for a collection of images at different locations). Subsequently, diamond-like carbon (DLC) coated tip has been used for high load measurements to avoid any wear at the tip apex (radius ~100 nm).

Wr in the graphene sheet show a significant contrast in the friction map (Figure 2a) which is quantitatively revealed by combining topographical and lateral force profile (Figure 2b). The trace and retrace scanning direction of the tip shows highest lateral force at the Wr and lowest value on 2LG with intermediate values on 1LG and at SE. The area under the

DOI: 10.1021/acsami.8b10294
ACS Appl. Mater. Interfaces 2018, 10, 44614−44623

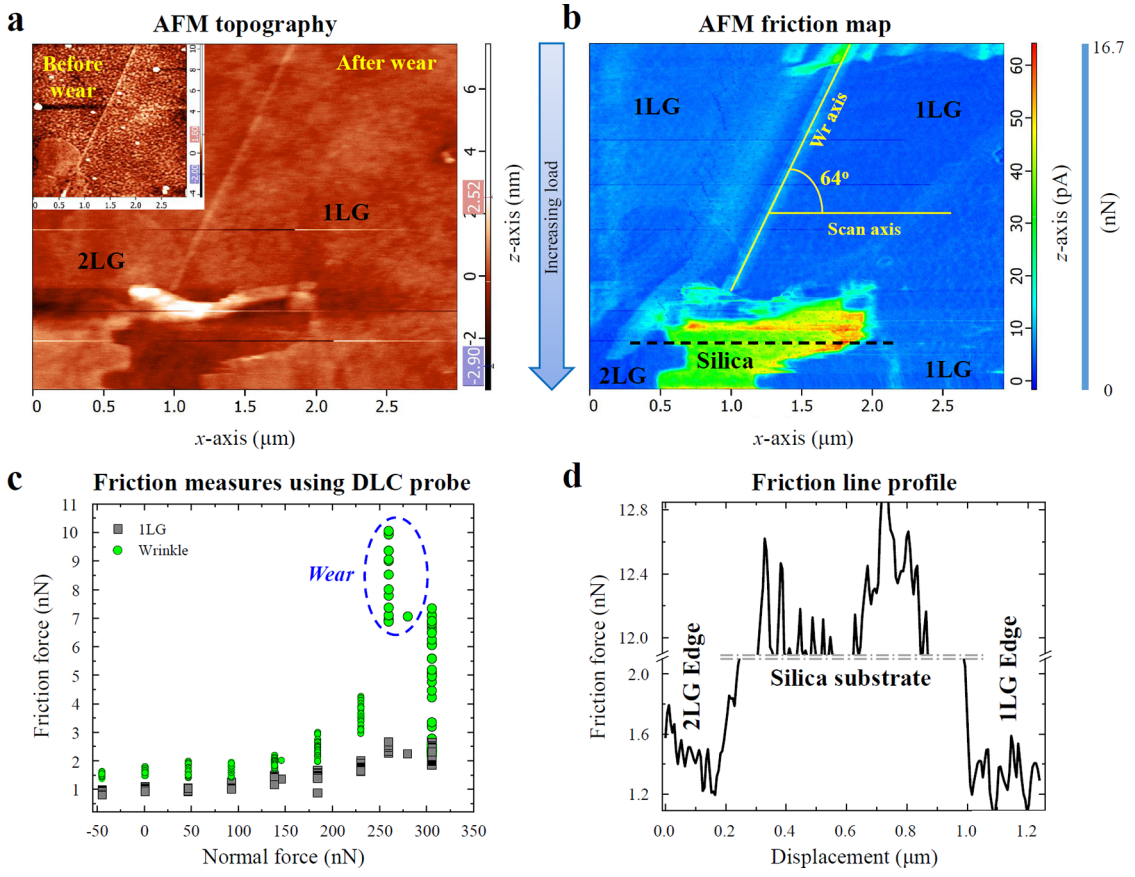

Figure 3. Surface wear of Wr and 1LG measured with DLC probes. (a) AFM topography of the CVD graphene before (inset) and after wear. (b) Friction map of the same region showing distribution of F_F along the Wr and 1LG. F_N is increased at intervals of 60 s from top to bottom direction (slow scan axis) up to wear of the Wr region. The orientation of the Wr is nearly 64° with respect to the fast scan axis of the cantilever. (c) F_F as a function of F_N in the 1LG region and at the Wr up to wear of the Wr occurring at F_N = 260 nN as marked by a sudden increase of F_F (dashed ellipse). Defect free 1LG shows lower F_F than the Wr for all F_N values in the analyzed range and no wear has been observed up to 300 nN. (d) Friction line profile referring to black dashed line in panel b.

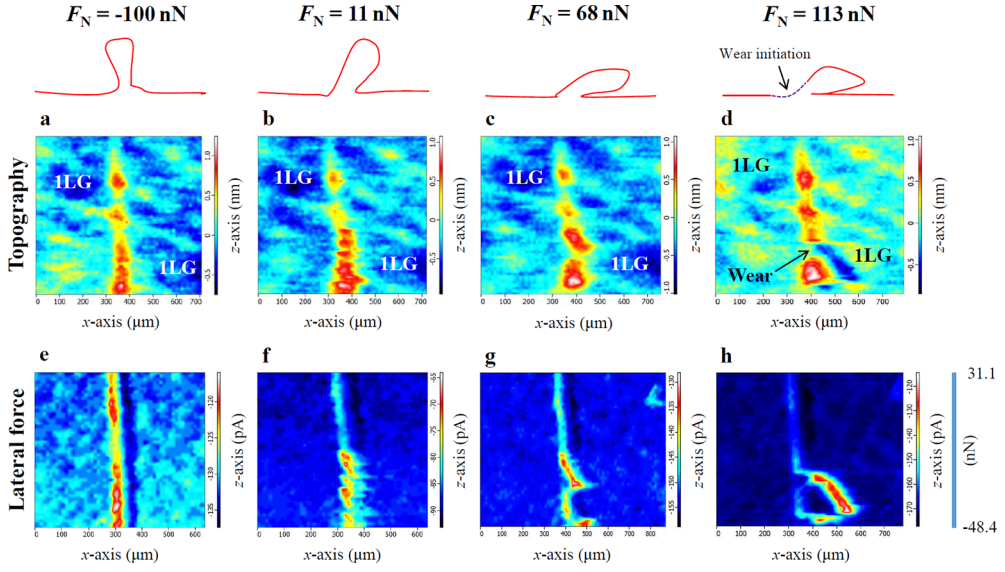

Figure 4. Deformation and wear of the vertical (standing) Wr in CVD graphene. Topography (a–d) and F_L map (e–h), with scanning direction from left to right, at increasing normal force, from −100 to 113 nN. The orientation of the wrinkle is nearly 90° with respect to the fast scanning direction. The height of the undeformed wrinkle, which is around 1 nm, changes at different F_N, indicating both normal and lateral deformations. The negative value of the F_L map is due to the use of single channel "trace". Wear has been observed only at the highest normal load of 113 nN.

DOI: 10.1021/acsami.8b10294
ACS Appl. Mater. Interfaces 2018, 10, 44614–44623

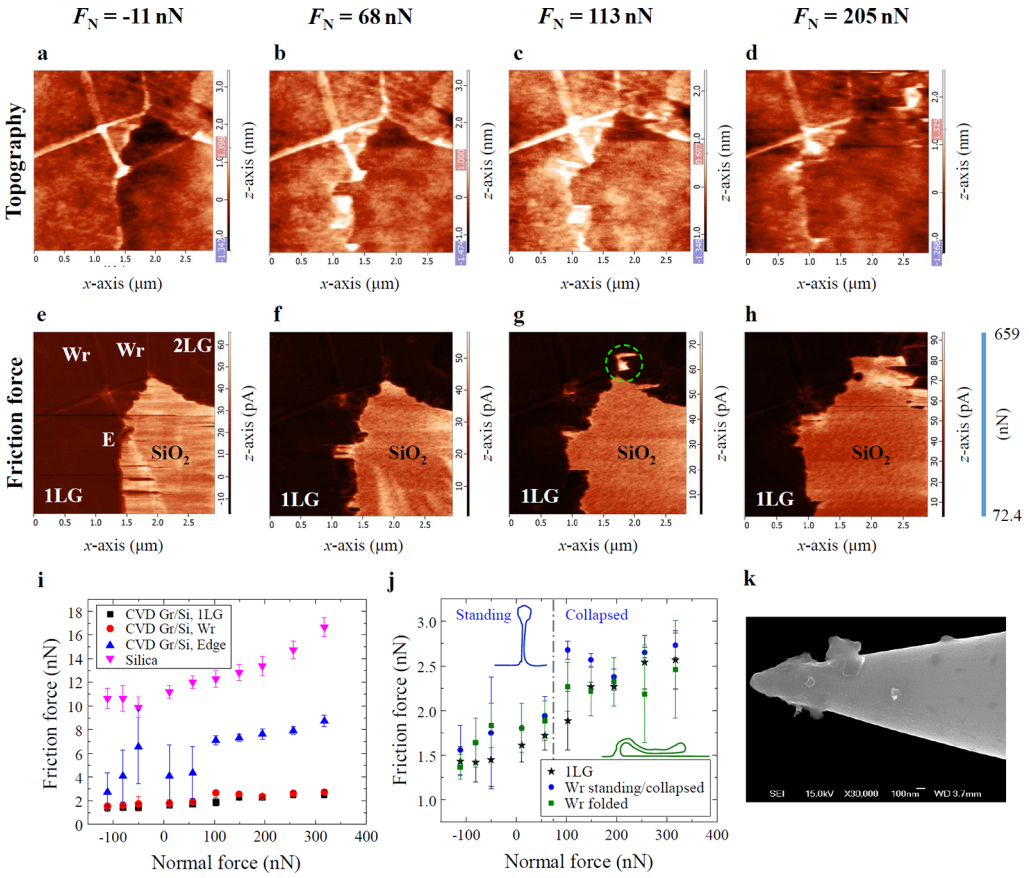

Figure 5. Topography, friction force maps, and dependence on normal load for E and horizontal and vertical Wr in CVD graphene. (a–d) AFM topography of CVD graphene over silica substrate at different applied loads. (e–h) Corresponding friction maps. The manipulation of graphene initiates from the E region and progresses up to the rupturing of Wr. (i) Load-dependent friction curves showing the trend of F_F at different F_N; silica substrate shows the highest F_F values while defect free basal graphene plane (1LG) has lowest F_F with intermediate values for the *E* and Wr. (j) Load-dependent friction of standing/collapsed and folded Wr (the vertical dashed line identifies the transition between standing and collapsed regime); the data from 1LG basal plane is used for comparison under the same F_N. (k) SEM image of the DLC tip after wear of the graphene sheet showing some graphene debris attached to the tip.

lateral force loop is associated with friction dissipation by the cantilever during sliding, which is highest at the Wr region. The frictional characteristics of the Wr depends on several factors: altitude, width, orientation to the fast scan axis and the normal force (F_N) applied. The analysis proposed in Figure 2c,d at constant load $F_N \approx 35$ nN compares different Wr orientations measured with the same tip condition. We obtained maximum value of the F_F for 2 nm amplitude Wr oriented at 90° with respect to the scanning axis and minimal value for Wr oriented nearly at 7°, showing the tendency to lower friction force toward parallel alignment of the Wr axis.

The orientation of the Wr has a significant impact on their friction and load bearing capabilities in sliding operations. Two examples are illustrated in Figure 3 and Figure 4, in which Wr axis is oriented to the scan axis of ~64° and ~90°, respectively. Under applied F_N range from −50 to 320 nN, Wr oriented at ~64° (Figure 3c) can bear a higher $F_N \approx 260$ nN than Wr oriented at ~90°, which has a critical $F_N \approx 113$ nN (Figure 4d,h). This suggests that the critical load scales with the component of F_F perpendicular to the Wr, which we may refer to as the cutting force.

The Wr axis oriented ~90° with respect to the cantilever scan direction is ideal to study the phenomenon of friction-induced deformation, because it induces the maximum deflection in the Wr. The topography and F_L maps are reported in Figure 4 for increasing F_N, i.e. equal to −100 nN (Figure 4a,e), 11 nN (b,f), 68 nN (c,g), and 113 nN (d,h), showing different extent of deflection up to wear for the highest normal load. At lower values of F_N, around −100 nN, where adhesion is prevailing, the wrinkle is more resistant to bending and traction and shows broader F_F distribution along its length (Figure 4a,e). With the increase of $F_N \approx 11$ nN, a lateral elastic deflection occurs toward the scanning direction of the tip (Figure 4b,f). At $F_N \approx 68$ nN several local folds, observed at 11 nN, merge into a larger global deflection, overcoming the inertia and the adhesion force with the substrate of the whole wrinkle (Figure 4c,g). At $F_N \approx 113$ nN (Figure 4d,h) initiation of wear is observed along the Wr axis, leading to significant increase of the F_F values as marked by black arrow. The schematic view illustrates the respective deflections of the Wr at different F_N and the wear initiated region. Nanoscale frictional characteristics of 1LG is associated with several factors such as substrate roughness,[37] electron–phonon coupling,[38] and the puckering effect, in which graphene elastically buckles in front of the sliding tip.[20] The presence of the Wr enhances the F_F due to its higher bending flexibility during the scanning of the cantilever as compared to the defect free 1LG for all applied F_N. We did not observe any wear in the defect free basal of 1LG in the applied load range.

DOI: 10.1021/acsami.8b10294
ACS Appl. Mater. Interfaces 2018, 10, 44614–44623

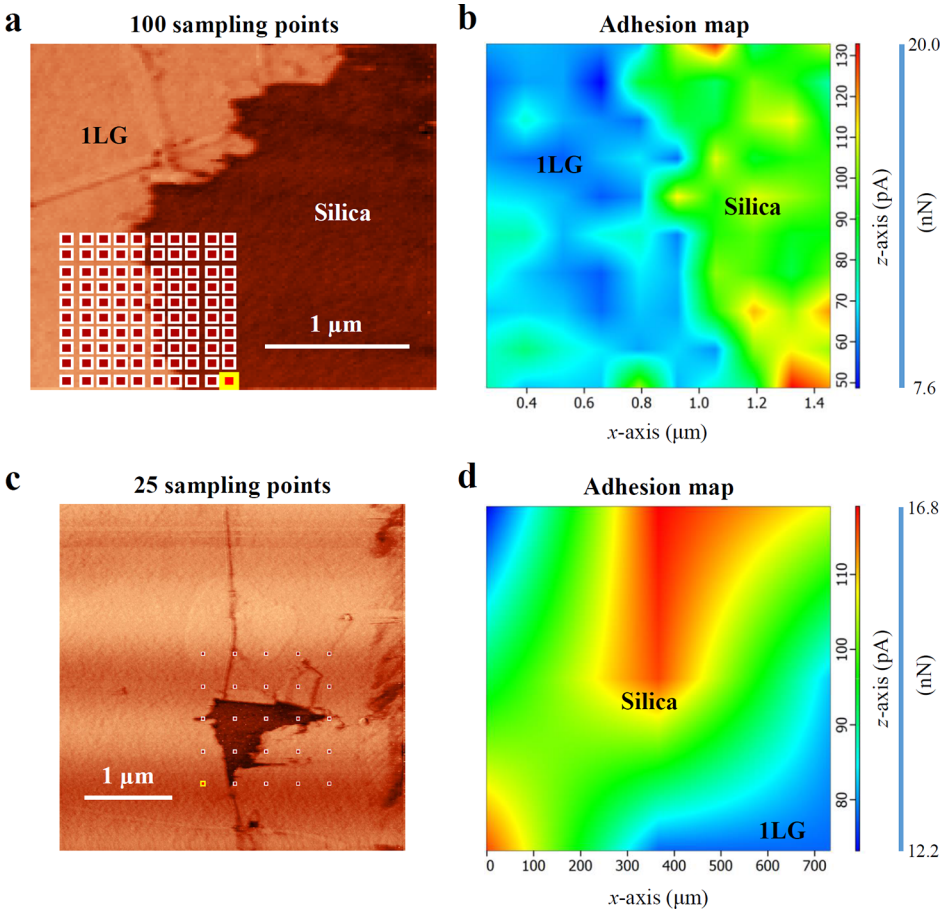

Figure 6. (a, b) Adhesion force map of 100 sampling points carried out over CVD graphene from silica substrate to 1LG. (c, d) Adhesion force map by interpolation of 25 sampling points of silica substrate surrounded by graphene. The color map shows the distribution of adhesion force which is highest at the silica region and lowest in 1LG.

The worn region of graphene appears to be the weakest site for further damage and rupturing due to the generation of the edges. The height of the edges relates to the friction signal. Thicker edges of 2LG have slightly higher friction than the 1LG edge as illustrated by friction line profile in Figure 3b,d and Figure S2a–d in the Supporting Information for both CVD and ME graphene, respectively. Nevertheless, the frictional characteristic of the graphene E is different from the Wr. The latter shows bending and stretching, while E and SE display folding and buckling mechanisms before wear that will be discussed in the present section. Here, we compare the F_F values for E, Wr, and defect free 1LG graphene in a single acquisition for different F_N values. Figure 5 shows topographies (a–d) and F_F maps (e–h) of Wrs (horizontal and vertical configurations), E, 1LG, and silica substrate under different F_N (namely, 11, 68, 113, and 205 nN). Initially, the wear of the graphene is observed in the *E* region at around 68 nN, for vertical wrinkle at 113 nN (marked by a dashed circle), whereas the horizontal Wr is unaffected even at the highest F_N of ∼320 nN, thus it is more robust against "cutting". The increment of F_N above 11 nN further removes the graphene carbon atoms from the E region via folding and tearing showing a "peel-induced rupture" mechanism.[39] F_F versus F_N values are reported in Figure 5i,j, showing highest F_F for the silica substrate and lowest for the CVD 1LG, with intermediate trends of Wr and E. This clearly shows the role of single layer graphene in reducing friction as solid-state lubricant, despite the possible presence of defects. In Figure 5j, the two different Wr topologies are compared in terms of F_F. Vertical Wr shows comparable F_F to the horizontal configuration for different F_N up to 200 nN of F_N. Nevertheless, horizontal (folded) Wr shows lower F_F at high load conditions (i.e., F_N > 200 nN) confirming its higher stability against rupture. This result can be explained with the fact that the horizontal wrinkle represents a postbending configuration of the vertical one, hence similar friction, but the topology of the first had higher time to relax and conform to the basal plane, hence higher stability is achieved at high normal loads.

The adhesion force maps measured from the silica substrate to the 1LG basal plane are reported in Figure 6 for two different regions showing higher values of adhesion force at the E region than 1LG. The measurement was carried out with force–distance spectroscopy by calculating pull-out forces. The average value of adhesion force for 1LG is measured as 9.18 ± 2.2 nN and at E region is 13 ± 2 nN. A hydrophilic surface like silica has higher affinity to deposit air-borne impurities and attract moisture (i.e., water molecules) also responsible for the higher adhesion force at E. Therefore, at the proximity of E, carbon atoms of graphene have a stronger interaction with the sliding probe[11] than basal plane graphene, leading to higher magnitude of friction as compared to 1LG and 2LG.[11] The absence of hexagonal symmetry at E regions makes them mechanically vulnerable during friction operations yeilding to elastic deformation, wrinkle formation, peeling and fracture.[19]

DOI: 10.1021/acsami.8b10294
ACS Appl. Mater. Interfaces 2018, 10, 44614–44623

Deng et al.[2] observed significant difference for the friction and adhesion forces for graphene-silica system between diamond and silica cantilevers. We observed similar behavior for both CVD and ME graphene (Figures S3−S5 in the Supporting Information). The obtained friction data are in close agreement with the measurements carried by Vasić et al.[19] The influence of air-borne impurities induced friction is also studied by a separate friction measurement in controlled nitrogen atmosphere, complemented with FEM simulation (Figure S6 in the Supporting Information). We obtained lower values of friction force in nitrogen conditions with respect to the air which validates the role of airborne impurities.

The trend of load dependent friction in Figures 3c and 5i (justifying vanishing F_F at negative values of F_N) is well described according to the following classical law[40]

$$F_F = \mu(F_N + F_A) + F_{Fo} \quad (1)$$

where, μ is the friction coefficient $\left(\frac{dF_F}{dF_N}\right)$, F_A is the adhesion force between the tip apex and graphene (measured from pull-out values) and F_{Fo} is the friction force recorded for $F_N + F_A = 0$ nN. The coefficient of friction values measured by linear fit of the F_F versus F_N curves of the structural defects are normalized by their corresponding for 1LG and are summarized in Table 1. A clear trend emerges in frictional characteristics of the structural defects depending on chemistry and shape of the tip (see Figure S7 in the Supporting Information) and the atmospheric conditions. All measurements are showing that E is more vulnerable in air conditions than SE and Wr, while 2LG can bear the highest normal force.

Table 1. Normalized Coefficient of Friction (μ) Values from Silica Substrate, E, SE, and Wr.[a]

μ_{sample}/μ_{1LG}	DLC probe (air)	Si probe (air)	Si probe (nitrogen)	FEM
silica substrate/1LG	5.33	13.46	9.78	-
E/1LG	4.00	3.84	1.30	1.46
SE/1LG	1.63	2.30	0.80	0.78
Wr/1LG	0.66	2.25	-	-
2LG/1LG	0.65	0.40	0.64	0.69

[a]Normalized to the corresponding defect-free 1LG in air/nitrogen conditions for different probes or related FEM predictions (assuming absence of air borne impurities, thus closer to nitrogen conditions, see Figure S6 in the Supporting Information).

Molecular dynamics simulation has been implemented to investigate the mechanical response of the SE with different range of normal force (F_{NS}, where the letter S denotes the simulation analogue of experiments) from 45 to 82 nN (Figure 7a,b) and from 80 nN to 128 nN (Figure 7c,d). The simulation setup is described in the Materials and Methods section and the top view of the setup is given in Figure S8 in the Supporting Information. In the subsequent stage of sliding, the probe and graphene terrace show lower F_{FS} than at SE (see a1 in Figure 7a). The friction is further increased due to a higher interaction of the tip atoms with the SE (see b1 in Figure 7a). Under given load range, the probe causes elastic folding of the graphene SE (see c1 in Figure 7a,b). Thus, enhanced friction force is generated due to out-of-plane deformation (see vertical height, Figure 7a) counteracting the van der Waals interaction between graphene sheets. Folding at c1 (Figure 7a,b) initiates for F_{NS} = 81.3 nN with F_{FS} = 39.6 nN. The friction decreases when the contact point of the probe passes over the folded SE atoms. At higher normal force range ($F_{NS} \approx$ 80 nN to 128 nN, see Figure 7c,d), the probe displaces the graphene SE, which in turn generates a buckled structure in the SE region. The friction force at the buckled SE regions is nearly 2.5 times higher than in 1LG basal plane.

The simulation setup comprises rigid boundary atoms which are artificially fixed and acted as constrained site. Hence, different values of F_{FS} can be obtained by changing the boundary conditions or the confinement, which affect the topography of the basal plane (see Figure S8 in the Supporting Information). Nevertheless, our simulation results illustrate that the buckling mechanism followed by the displacement of SE atoms might be a precursor for tearing at the step edge (see SI video). Quantitative measure of the structural defect opposition to the lateral movement of the probe is given by the cumulative work of the probe during its sliding motion, determined as follows:

$$W = \frac{1}{2}\sum_{i=1}^{n}(L_i + L_{i-1})(x_i - x_{i-1}) \quad (2)$$

where, L_i is the lateral force corresponding to the current X_i displacement of the probe. For Figure 7a it is calculated as 0.564 keV, whereas for Figure 7c is 1.153 keV. This result shows that the work carried out by the probe to fold graphene step atoms is about a half of the value for buckling and tearing.

CONCLUSION

Typical structural defects in 2D materials, namely E, SE, and Wr, were scanned through AFM at different normal force levels in both ME and CVD graphene samples. Lateral deformation appeared higher at E than at SE regions for the ME graphene. The deformation may yield into folding, buckling and tearing, according to load conditions and defect type as demonstrated by MD and FEM simulations. SE exhibited the highest normal forces up to F_N = 74 nN while wear initiated in E at around F_N = 57 nN. It is shown that the basal layer of graphene significantly contributes in the load and friction bearing capacity of a line defect. Airborne impurities might also enhance the interaction between probe apex and the SE atoms, affecting friction measurements. A trend of increasing friction coefficient from 1LG to E and SE clearly emerges. All these factors lead to the detrimental effect on loading bearing capacity of the E and SE regions. Nevertheless, the role of impurities and its effect on the tribological characteristics of such defects is worthy for further investigations.

In CVD graphene, horizontal Wr was found to be more robust than vertical ones, whereas E was the weakest defect against friction and normal forces. For Wr, the initiation of wear appears at the interface between 1LG and Wr. Using DLC and Si tips, we found that the CVD graphene is a more mechanically robust protective coating under sliding operation than ME graphene due to the minimal presence of E and SE in the former category.

MATERIALS AND METHODS

Natural graphite was used as a source of graphene layers, which was mechanically peeled off through scotch tape method and physically deposited over silica substrate (300 nm oxide layer). The produced sample was annealed in argon atmosphere at 450 °C for 3 h to remove organic impurities. The number of atomic layers of graphene were determined through Raman spectroscopy (Horiba, Jobin-Yvon spectrometer model: Labram, 632.8 nm wavelength, spot diameter

DOI: 10.1021/acsami.8b10294
ACS Appl. Mater. Interfaces 2018, 10, 44614−44623

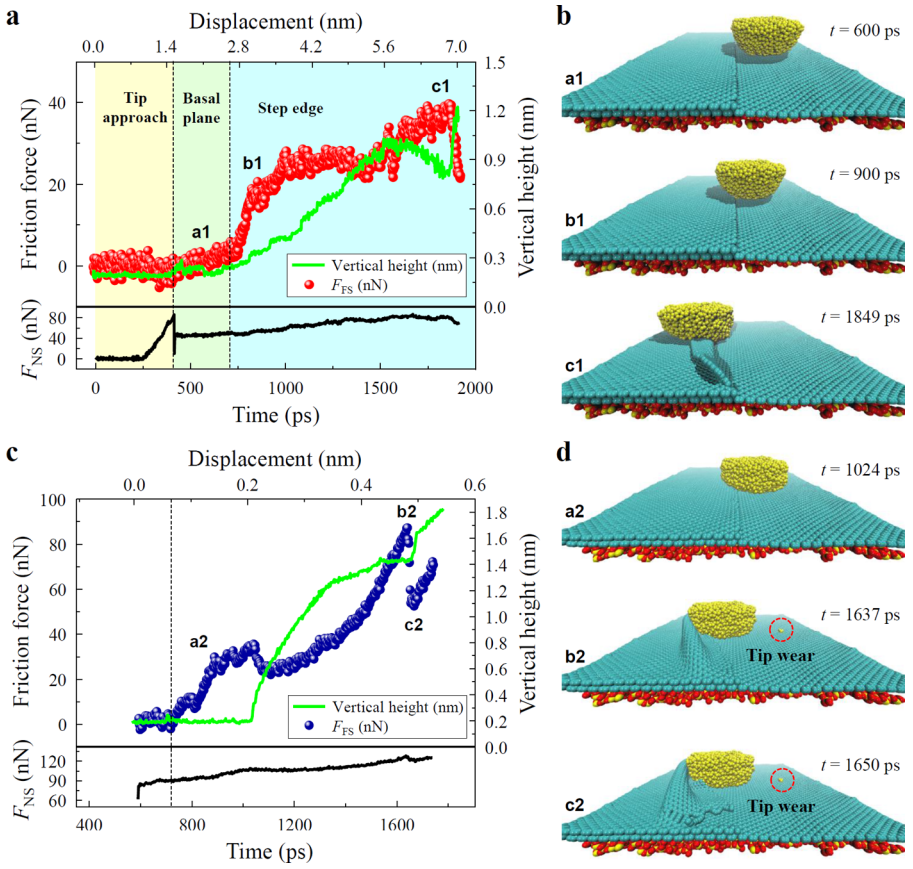

Figure 7. MD simulated friction force profiles and related configurations of SE scanning at two different normal force ranges. (a) In the lower panel the normal force along the entire tip scan is reported. The vertical dashed line identifies the position of the E. (b) Snapshots of three conditions (a1, b1, and c1) given in panel (a). (c) At higher normal force range, "buckling" (starting just after a2) followed by tearing (at b2) of SE are observed. After tearing, the friction force drops (b2 to c2). (d) Snapshots of the three conditions (a2, b2, and c2) given in panel (c), also showing tip wear.

~3−4 μm). CVD graphene over silicon sample (Gr/Si-CVD) was commercially obtained from Graphenea (Graphenea Inc., Spain).

AFM measurements in nitrogen condition were carried out as follows: the graphene sample was inserted into an AFM setup (commercial Enviroscope system by VEECO) with optional sample heater (Enviroscope P/N: ESHTH), controlled by the Nanoscope IV unit. The AFM chamber was connected with a turbomolecular pump and an oil-free scroll vacuum pump to carry out measurements in high vacuum (10^{-5} Torr). The sample was heated inside the AFM chamber at 150 °C for 2 h in vacuum. After the cooling of the AFM chamber in vacuum, nitrogen flux was introduced into the AFM chamber to carry out FFM measurement in nitrogen atmosphere. FFM measurement was also carried out in air condition using Solver P47H from NT-MDT in contact mode operation using lateral force channel for forward and backward direction.

Commercially available silicon tips PFQNE_AL from Bruker, (MikroMasch model No. CSC37/noAl, NT-MDT model No. CSG01, NSG10) and DCP01 (silicon probe coated with diamond-like coating) have been used for the topographic analysis and friction measurements. Force−distance (F−D) curves were carried out over Si wafer to measure the sensitivity of the photodetector that allows conversion of units from volts/ampere to nanometers using the slope of the forward part of the curve. The comprehensive detail of the procedure can be found elsewhere.[41] The cantilevers were calibrated by following the Sader method[42,43] to measure their normal and lateral spring constants. The bending and torsional elastic stiffness of the cantilevers were measured ~0.4 N/m and between 2−3 10^{-8} Nm, respectively. Lateral force (F_L) was derived from the twisting of cantilever during scanning which was deduced from the lateral photodetector voltage following the procedure described elsewhere[41,44] with the assumption of the circular shape of laser beam on the photo detector. We refer F_F values as the spatial mean of F_L recorded after scanning of tip in forward and reverse direction. In that calculation, lateral sensitivity of photodetector was assumed to be equal to the sensitivity measured in normal bending of cantilever.

Before performing FFM measurement, the sample was mechanically cleaned in the AFM in contact mode by a different cantilever. Three different graphene flakes have been used for testing in air condition for ME graphene and four different regions have been explored over polycrystalline sample (Gr/Si-CVD). The FFM measurement was carried out on an area of 1 × 1 μm^2 to 3 × 3 μm^2 while systematically increasing normal force. This procedure allowed to analyze 1LG, 2LG, SE, and silica in the same acquisition, useful to carry out comparative studies. After each session of the FFM, F−D curves were performed for pull-off measurements and later cantilevers were passed through silicon grating sample (Model TGT1) to monitor the shape of the tips.

SEM was carried out over Gr/Si-CVD sample using NOVA Instrument operated in SED mode at 10 kV.

The FEM model has been developed in order to reproduce a continuous scan from silica substrate to 2LG, passing through E and SE (Figure S6 in the Supporting Information). The substrate and the tip were modeled with solid elements while the graphene flake via shell elements (thickness of one layer equal to 0.066 nm = 0.34/5 nm to properly account the actual bending stiffness of the layer[45]). The molecular van der Waals interaction between all the bodies of the model (tip with flake and substrate, flake and substrate, graphene layers) were modeled via a cohesive zone model based on the Lennard-Jones 6-12 potential (more details are reported in the Supporting Information).[46] The tip, is subjected to imposed F_N, could

DOI: 10.1021/acsami.8b10294
ACS Appl. Mater. Interfaces 2018, 10, 44614−44623

slide in the horizontal, being a constant translational velocity imposed towards E and SE (rotation of the simulated AFM tip is not permitted). Friction force was determined by computing the component of the contact force on the tip ($F_L = F_F$) parallel to scanning motion.

The MD simulations were carried out using the ReaxFF force field[47] implemented in the LAMMPS package[48] at 300 K using a time step of 0.5 fs. The tip was made by 4099 silicon atoms packed in a ∼30 Å radius hemisphere. Its top part (1171 atoms) was considered as a rigid body whereas its bottom part (2928 atoms) contained atoms that could move freely. The tip was moved using three different springs which were attached in one extremity to the center of mass of the rigid body and in another extremity to external points on the *x*-, *y*-, and *z*-axes, respectively. The spring constants were 500 kcal/(mol·Å^2) in the horizontal plane (*x* and *y*) and 800 kcal/(mol·Å^2) in the vertical spring (*z*). Moving the attachment point with a constant velocity (0.5×10^{-5}nm/fs in our simulations) allowed us to measure the interaction force between the tip and the surface which corresponds to the experienced force by the spring in that direction. To avoid the rotation of the tip, its angular momentum was set to zero at every simulation step. The silica substrate was formed by ∼11000 atoms packed in 150 Å × 150 Å × 20 Å flake which was first minimized and then thermalized using the NVT ensemble for 400 ps. After that, the graphene sheet formed by ∼13000 atoms was mounted on the substrate and thermalized for 400 ps using NPT ensemble keeping the external pressure null in the periodic direction to avoid any kind of initial stress. Due to the network mismatch between the graphene sheet and the substrate, the substrate was built slightly shorter than the graphene sheet. The silicon tip was minimized and thermalized in the NVT ensemble for 400 ps. Then, the sliding simulation begins using the NVT ensemble and keeping the silica substrate and the graphene borders fixed. First, the tip starts to lower down toward the substrate until the desired normal force achieved between the tip and the surface. Sequentially, the tip starts to move orthogonally to the edge axis in MD simulations; we fixed the border to prevent translation of the graphene sheet under the force of the tip. This translation is prevented in the experiments by interactions between graphene and the substrate in regions where graphene is not suspended (simulating this entire setup is beyond the capabilities of computational infrastructure). By reducing the size of the graphene flake, we also accelerated the entire duration of fracture process.

■ ASSOCIATED CONTENT

Supporting Information

The Supporting Information is available free of charge on the ACS Publications website at DOI: 10.1021/acsami.8b10294.

Topography of CVD graphene wrinkles with different cantilevers. Topography and roughness distribution of ME and CVD graphene by AFM, Raman spectroscopy of ME 1LG and 2LG. Topography, friction force map and load dependent friction curves of ME graphene flake in air condition. Intermittent contact mode image from the E and SE after FFM measurements and detail of broken step edge. Friction and adhesion maps of a second ME graphene flake. Section profile of different tip apexes. Set-up of finite element method and molecular dynamics simulations scans from silica substrate to 2LG (PDF)

MD simulation of different phenomena of deformation of the step edge region under different applied normal force (AVI)

■ AUTHOR INFORMATION

Corresponding Author

*E-mail: nicola.pugno@unitn.it.

ORCID

Manoj Tripathi: 0000-0002-8052-428X
Stefano Signetti: 0000-0003-4128-0953
Alan Dalton: 0000-0001-8043-1377
Nicola Maria Pugno: 0000-0003-2136-2396

Notes

The authors declare no competing financial interest.

■ ACKNOWLEDGMENTS

N.M.P. is supported by the European Commission under the Graphene Flagship Core 2 no. 785219 (WP14 "Composites") and FET Proactive "Neurofibers" no. 732344 as well as by the MIUR with the "Departments of Excellence" Grant L. 232/2016 and ARS01-01384-PROSCAN. M.T. would like to acknowledge University of Sussex strategic developement fund and thankfull to Mario Barozzi for providing SEM images. G.P. and S.V. would like to acknowledge Regione Emilia Romagna, Project INTERMECH−MO.RE and EU COST program under Action MP1303. F.A. would like to acknowledge the financial support of the FWF Lise Meitner program, project M1777. S.S. acknowledges financial support from Ermenegildo Zegna Founder's Scholarship 2017-2018.

■ REFERENCES

(1) Feng, X.; Kwon, S.; Park, J. Y.; Salmeron, M. Superlubric Sliding of Graphene Nanoflakes on Graphene. *ACS Nano* **2013**, *7* (2), 1718−1724.

(2) Deng, Z.; Klimov, N. N.; Solares, S. D.; Li, T.; Xu, H.; Cannara, R. J. Nanoscale Interfacial Friction and Adhesion on Supported versus Suspended Monolayer and Multilayer Graphene. *Langmuir* **2013**, *29* (1), 235−243.

(3) Klemenz, A.; Pastewka, L.; Balakrishna, S. G.; Caron, A.; Bennewitz, R.; Moseler, M. Atomic Scale Mechanisms of Friction Reduction and Wear Protection by Graphene. *Nano Lett.* **2014**, *14* (12), 7145−7152.

(4) Wählisch, F.; Hoth, J.; Held, C.; Seyller, T.; Bennewitz, R. Friction and atomic-layer-scale wear of graphitic lubricants on SiC(0001) in dry sliding. *Wear* **2013**, *300* (1−2), 78−81.

(5) Shin, Y. J.; Stromberg, R.; Nay, R.; Huang, H.; Wee, A. T. S.; Yang, H.; Bhatia, C. S. Frictional characteristics of exfoliated and epitaxial graphene. *Carbon* **2011**, *49* (12), 4070−4073.

(6) Kim, K. S.; Lee, H. J.; Lee, C.; Lee, S. K.; Jang, H.; Ahn, J. H.; Kim, J. H.; et al. Chemical vapor deposition-grown graphene: the thinnest solid lubricant. *ACS Nano* **2011**, *5* (6), 5107−5114.

(7) Sandoz-Rosado, E. J.; Tertuliano, O. A.; Terrell, E. J. An atomistic study of the abrasive wear and failure of graphene sheets when used as a solid lubricant and a comparison to diamond-like-carbon coatings. *Carbon* **2012**, *50* (11), 4078−4084.

(8) Vasić, B.; Zurutuza, A.; Gajić, R. Spatial variation of wear and electrical properties across wrinkles in chemical vapour deposition graphene. *Carbon* **2016**, *102*, 304−310.

(9) Long, F.; Yasaei, P.; Yao, W.; Salehi-Khojin, A.; Shahbazian-Yassar, R. Anisotropic Friction of Wrinkled Graphene Grown by Chemical Vapor Deposition. *ACS Appl. Mater. Interfaces* **2017**, *9* (24), 20922−20927.

(10) Huang, P. Y.; Ruiz-Vargas, C. S.; van der Zande, A. M.; Whitney, W. S.; Levendorf, M. P.; Kevek, J. W.; Garg, S.; Alden, J. S.; Hustedt, C. J.; Zhu, Y.; Park, J.; McEuen, P. L.; Muller, D. A. Grains and grain boundaries in single-layer graphene atomic patchwork quilts. *Nature* **2011**, *469* (7330), 389−392.

(11) Lee, H.; Lee, H.-B.-R.; Kwon, S.; Salmeron, M.; Park, J. Y. Internal and External Atomic Steps in Graphite Exhibit Dramatically Different Physical and Chemical Properties. *ACS Nano* **2015**, *9* (4), 3814−3819.

DOI: 10.1021/acsami.8b10294
ACS Appl. Mater. Interfaces 2018, 10, 44614−44623

(12) Zhang, J.; Zhao, J.; Lu, J. Intrinsic Strength and Failure Behaviors of Graphene Grain Boundaries. *ACS Nano* **2012**, *6* (3), 2704−2711.
(13) Ruiz-Vargas, C. S.; Zhuang, H. L.; Huang, P. Y.; van der Zande, A. M.; Garg, S.; McEuen, P. L.; Muller, D. A.; Hennig, R. G.; Park, J. Softened Elastic Response and Unzipping in Chemical Vapor Deposition Graphene Membranes. *Nano Lett.* **2011**, *11* (6), 2259−2263.
(14) Han, J.; Pugno, N. M.; Ryu, S. Nanoindentation cannot accurately predict the tensile strength of graphene or other 2D materials. *Nanoscale* **2015**, *7* (38), 15672−15679.
(15) Androulidakis, C.; Koukaras, E. N.; Frank, O.; Tsoukleri, G.; Sfyris, D.; Parthenios, J.; Pugno, N.; Papagelis, K.; Novoselov, K. S.; Galiotis, C. Failure processes in embedded monolayer graphene under axial compression. *Sci. Rep.* **2015**, *4*, 5271.
(16) Pugno, N. M. The elasticity and strength of graphene. *Recent Res. Devel. Mater.Sci.* **2009**, *8*, 101−103.
(17) Qi, Z.; Cao, P.; Park, H. S. Density functional theory calculation of edge stresses in monolayer MoS2. *J. Appl. Phys.* **2013**, *114* (16), 163508.
(18) Suenaga, K.; Koshino, M. Atom-by-atom spectroscopy at graphene edge. *Nature* **2010**, *468* (7327), 1088−1090.
(19) Vasić, B.; Matković, A.; Gajić, R.; Stanković, I. Wear properties of graphene edges probed by atomic force microscopy based lateral manipulation. *Carbon* **2016**, *107*, 723−732.
(20) Lee, C.; Li, Q.; Kalb, W.; Liu, X. Z.; Berger, H.; Carpick, R. W.; Hone, J. Frictional characteristics of atomically thin sheets. *Science* **2010**, *328* (5974), 76−80.
(21) Dong, Y.; Liu, X. Z.; Egberts, P.; Ye, Z.; Carpick, R. W.; Martini, A. Correlation Between Probe Shape and Atomic Friction Peaks at Graphite Step Edges. *Tribol. Lett.* **2013**, *50* (1), 49−57.
(22) Fajardo, O. Y.; Mazo, J. J. Surface defects and temperature on atomic friction. *J. Phys.: Condens. Matter* **2011**, *23* (35), 355008.
(23) Meyer, E.; Lüthi, R.; Howald, L.; Bammerlin, M.; Guggisberg, M.; Güntherodt, H. J. Site-specific friction force spectroscopy. *J. Vac. Sci. Technol., B: Microelectron. Process. Phenom.* **1996**, *14* (2), 1285−1288.
(24) Overney, R. M.; Meyer, E.; Frommer, J.; Brodbeck, D.; Luthi, R.; Howald, L.; Giintherodt, H. J.; Fujihira, M.; Takano, H.; Gotoh, Y. Friction measurements on phase-separated thin films with a modified atomic force microscope. *Nature* **1992**, *359* (6391), 133−135.
(25) Egberts, P.; Han, G. H.; Liu, X. Z.; Johnson, A. T. C.; Carpick, R. W. Frictional Behavior of Atomically Thin Sheets: Hexagonal-Shaped Graphene Islands Grown on Copper by Chemical Vapor Deposition. *ACS Nano* **2014**, *8* (5), 5010−5021.
(26) Ye, Z.; Martini, A. Atomic friction at exposed and buried graphite step edges: experiments and simulations. *Appl. Phys. Lett.* **2015**, *106* (23), 231603.
(27) Yu, S. U.; Park, B.; Cho, Y.; Hyun, S.; Kim, J. K.; Kim, K. S. Simultaneous visualization of graphene grain boundaries and wrinkles with structural information by gold deposition. *ACS Nano* **2014**, *8* (8), 8662−8668.
(28) Cannara, R. J.; Brukman, M. J.; Cimatu, K.; Sumant, A. V.; Baldelli, S.; Carpick, R. W. Nanoscale friction varied by isotopic shifting of surface vibrational frequencies. *Science* **2007**, *318* (5851), 780−3.
(29) Li, Q.; Tullis, T. E.; Goldsby, D.; Carpick, R. W. Frictional ageing from interfacial bonding and the origins of rate and state friction. *Nature* **2011**, *480* (7376), 233−236.
(30) Weymouth, A. J.; Hofmann, T.; Giessibl, F. J. Quantifying Molecular Stiffness and Interaction with Lateral Force Microscopy. *Science* **2014**, *343* (6175), 1120−1122.
(31) Dietzel, D.; Mönninghoff, T.; Herding, C.; Feldmann, M.; Fuchs, H.; Stegemann, B.; Ritter, C.; Schwarz, U. D.; Schirmeisen, A. Frictional duality of metallic nanoparticles: Influence of particle morphology, orientation, and air exposure. *Phys. Rev. B: Condens. Matter Mater. Phys.* **2010**, *82* (3), 035401.
(32) Ternes, M.; Lutz, C. P.; Hirjibehedin, C. F.; Giessibl, F. J.; Heinrich, A. J. The Force Needed to Move an Atom on a Surface. *Science* **2008**, *319* (5866), 1066−1069.
(33) Hölscher, H.; Ebeling, D.; Schwarz, U. D. Friction at Atomic-Scale Surface Steps: Experiment and Theory. *Phys. Rev. Lett.* **2008**, *101* (24), 246105.
(34) Sundararajan, S.; Bhushan, B. Topography-induced contributions to friction forces measured using an atomic force/friction force microscope. *J. Appl. Phys.* **2000**, *88* (8), 4825.
(35) Demirbaş, T.; Baykara, M. Z. Nanoscale tribology of graphene grown by chemical vapor deposition and transferred onto silicon oxide substrates. *J. Mater. Res.* **2016**, *31* (13), 1914−1923.
(36) Malard, L. M.; Pimenta, M. A.; Dresselhaus, G.; Dresselhaus, M. S. Raman spectroscopy in graphene. *Phys. Rep.* **2009**, *473* (5−6), 51−87.
(37) Ye, Z.; Balkanci, A.; Martini, A.; Baykara, M. Z. Effect of roughness on the layer-dependent friction of few-layer graphene. *Phys. Rev. B: Condens. Matter Mater. Phys.* **2017**, *96* (11), 115401.
(38) Filleter, T.; McChesney, J.; Bostwick, A.; Rotenberg, E.; Emtsev, K.; Seyller, T.; Horn, K.; Bennewitz, R. Friction and Dissipation in Epitaxial Graphene Films. *Phys. Rev. Lett.* **2009**, *102* (8), 086102.
(39) Qi, Y.; Liu, J.; Zhang, J.; Dong, Y.; Li, Q. Wear Resistance Limited by Step Edge Failure: The Rise and Fall of Graphene as an Atomically Thin Lubricating Material. *ACS Appl. Mater. Interfaces* **2017**, *9* (1), 1099−1106.
(40) Gao, J.; Luedtke, W. D.; Gourdon, D.; Ruths, M.; Israelachvili, J. N.; Landman, U. Frictional Forces and Amontons' Law: From the Molecular to the Macroscopic Scale. *J. Phys. Chem. B* **2004**, *108* (11), 3410−3425.
(41) Carpick, R. W.; Salmeron, M. Scratching the Surface: Fundamental Investigations of Tribology with Atomic Force Microscopy. *Chem. Rev.* **1997**, *97* (4), 1163−1194.
(42) Sader, J. E.; Chon, J. W. M.; Mulvaney, P. Calibration of rectangular atomic force microscope cantilevers. *Rev. Sci. Instrum.* **1999**, *70* (10), 3967.
(43) Green, C. P.; Lioe, H.; Cleveland, J. P.; Proksch, R.; Mulvaney, P.; Sader, J. E. Normal and torsional spring constants of atomic force microscope cantilevers. *Rev. Sci. Instrum.* **2004**, *75* (6), 1988.
(44) Bachmann, D.; Hierold, C. Determination of pull-off forces of textured silicon surfaces by AFM force curve analysis. *J. Micromech. Microeng.* **2007**, *17* (7), 1326−1333.
(45) Scarpa, F.; Adhikari, S.; Gil, A.; Remillat, C. The bending of single layer graphene sheets: the lattice versus continuum approach. *Nanotechnology* **2010**, *21* (12), 125702.
(46) Jiang, L. Y.; Huang, Y.; Jiang, H.; Ravichandran, G.; Gao, H.; Hwang, K.; Liu, B. A cohesive law for carbon nanotube/polymer interfaces based on the van der Waals force. *J. Mech. Phys. Solids* **2006**, *54* (11), 2436−2452.
(47) van Duin, A. C. T.; Dasgupta, S.; Lorant, F.; Goddard, W. A. ReaxFF: A Reactive Force Field for Hydrocarbons. *J. Phys. Chem. A* **2001**, *105* (41), 9396−9409.
(48) Plimpton, S. Fast parallel algorithms for short-range molecular dynamics. *J. Comput. Phys.* **1995**, *117* (1), 1−19.

NOTE ADDED AFTER ASAP PUBLICATION

This paper was published on the Web on December 13, 2018. Reference citations 7 and 12 were removed from the last paragraph of the paper, and the corrected version was reposted on December 14, 2018.

DOI: 10.1021/acsami.8b10294
ACS Appl. Mater. Interfaces 2018, 10, 44614−44623

Friction and adhesion of different structural defects of graphene

- Supporting Information -

Manoj Tripathi[a], Firas Awaja[b], Rafael A. Bizao[c], Stefano Signetti[d], Erica Iacob[e], Guido Paolicelli[f], Sergio Valeri[f,g], Alan Dalton[a], Nicola Maria Pugno[c,h,i,*]

[a]*Department of Mathematics and Physical Sciences, University of Sussex, Brighton BN1 9RH, United Kingdom*

[b]*Department of Orthopaedic Surgery, Medical University Innsbruck, Innrain 36, Innsbruck, Austria*

[c]*Laboratory of Bio-Inspired & Graphene Nanomechanics, Department of Civil, Environmental and Mechanical Engineering, University of Trento, via Mesiano 77, I-38123 Trento, Italy*

[d]*Department of Mechanical Engineering, Korea Advanced institute of Science and Technology (KAIST), 291 Daehak-ro, Yuseong-gu, Daejeon 34141, Republic of Korea*

[e]*Centre for Materials and Microsystems, Fondazione Bruno Kessler, via Sommarive 18, I-38123 Trento, Italy*

[f]*Istituto Nanoscienze, Consiglio Nazionale delle Ricerche, via G. Campi 213/a, 41125- Modena, Italy*

[g]*Dipartimento di Scienze Fisiche Informatiche e Matematiche (FIM), Università di Modena e Reggio Emilia, via Campi 213/a, I-41125 Modena, Italy*

[h]*School of Engineering and Materials Science, Queen Mary University of London, Mile End Road, E1 4NS London, United Kingdom*

[i]*KetLab, Edoardo Amaldi Foundation, via del Politecnico snc, I-00133 Roma, Italy*

*Corresponding author: nicola.pugno@unitn.it

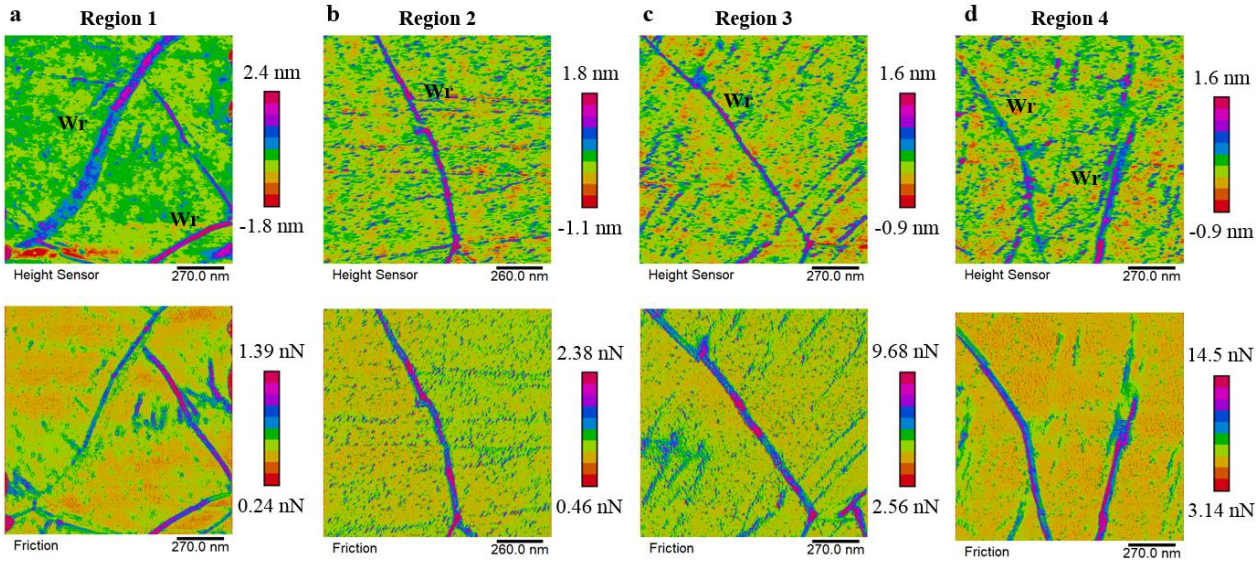

Figure S1. Topography (upper row) and frictional force (lower row) characteristics of CVD graphene wrinkles as compared to the sorrounding graphene basal plane (1LG) obtained at different locations from different cantilevers. Cantilever of stiffness K_n = 1.3 N/m for the panels (a, b) and K_n = 2.6 N/m for the panels (c, d) were used for the friction force measurements. Wrinkles of different altitude, orientation, and width show a contrast in friction force as compared to 1LG. The scale bar clearly differentiates the higher altitude of the wrinkles responsible for the larger friction force recorded by the cantilevers.

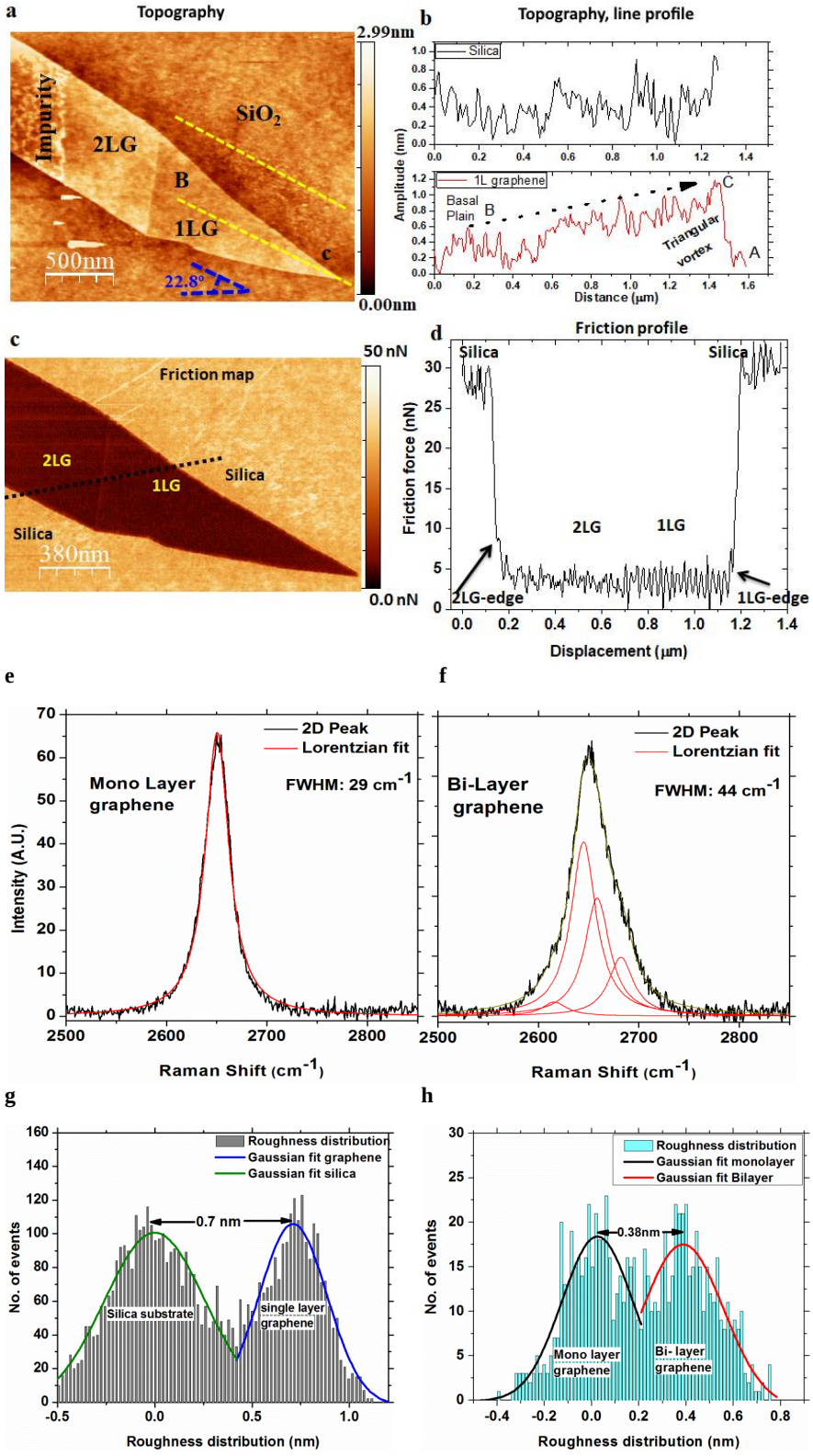

Figure S2. (a) AFM topographic image (intermittent contact mode) of ME graphene after mechanical cleaning in contact mode operation. The brighter color in AFM topography represents more elevated graphene from the substrate. This is validated by the 2LG line profile over silica surface parallel to the

axis of the graphene sheet. The altitude of 1LG increases from the basal plane (point B) to the vertex (point C) from 0.2 nm to 1.2 nm. (b) Topography profile of silica surface parallel to the line profile on 1LG shows constant height, thus the absence of any artefact from the substrate. The measure shows that graphene edge region along the vertex has lower interaction with silica substrate as compared to the basal plane. (c) Friction map of ME graphene showing friction contrast at the 2LG, 1LG, SE, and E for fixed F_N. (d) Friction line profile along 2LG-edge to 1LG-edge showing slight differences in the F_F, which corresponds in altitude to the passage through the edge. (e, f) Raman spectra of 2D peak for 1LG (~ 2651 cm^{-1}) and 2LG (2654 cm^{-1}), respectively. The monolayer is fitted with a single Lorentzian curve with the full width half maximum (FWHM) ~ 29 cm^{-1} and the bi-layer is fitted with four Lorentzian curves[1]. (g, h) Roughness distribution of 1LG over silica substrate and 1LG-2LG is used to measure the thickness of graphene layer/s. The Gaussian fit of the roughness distribution provides the average altitude difference between 1LG-silica and 1LG-2LG, being 0.7 nm and 0.38 nm respectively.

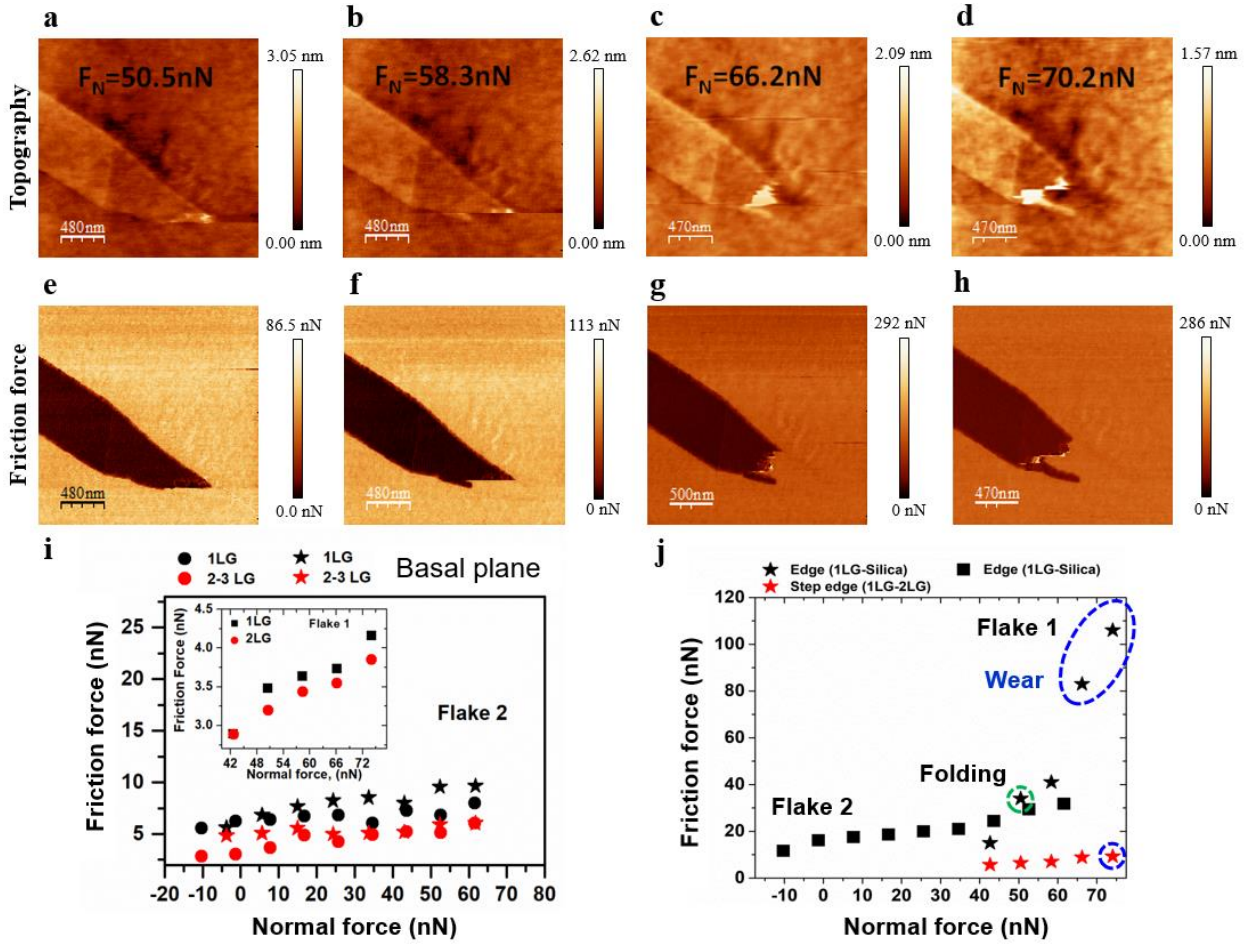

Figure S3. Topography and friction force maps at different normal load (from 50 to 70 nN) for E and SE in ME graphene yielding to (a) cutting of the folded graphene, (b) tearing and (c, d) wear. The corresponding friction force (F_F) maps are shown in panels (e-h). (i) F_F vs F_N for the two different basal planes (ME graphene flakes no. 1 and 2) for 1LG, and 2LG (repeated twice). 1LG shows higher friction force than 2LG in the whole range of tested normal forces. (j) F_F vs F_N for E and SE, highlighting deformations in graphene flakes, i.e. folding (green dashed circle) and wear (blue dashed circle). The F_F increases with F_N and deformation occurs at the E region by folding (panels a, e), cutting (panels b, f) and wear (panels d, h). The 2LG surface shows the lowest friction forces for all applied F_N whereas E the highest values. The tearing of E is observed at $F_N \approx 58$ nN and for SE at ≈ 74 nN.

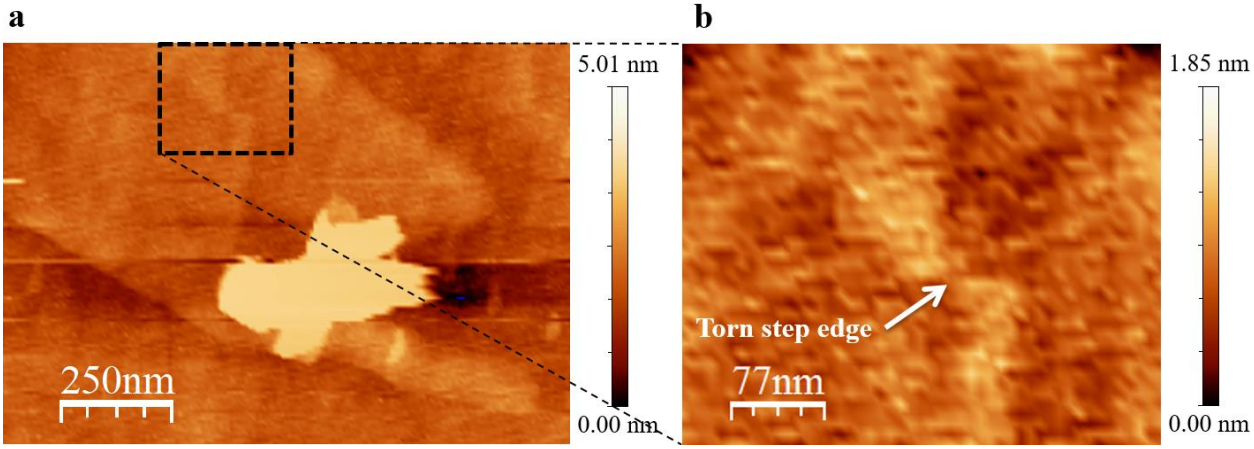

Figure S4. AFM Topography of ME flake nr. 1. (a) Intermittent contact mode carried out after FFM operations showing rupture of the edge and initiation of tearing at the step-edge for fixed normal load of 74 nN. (b) Magnified region around the broken step edge.

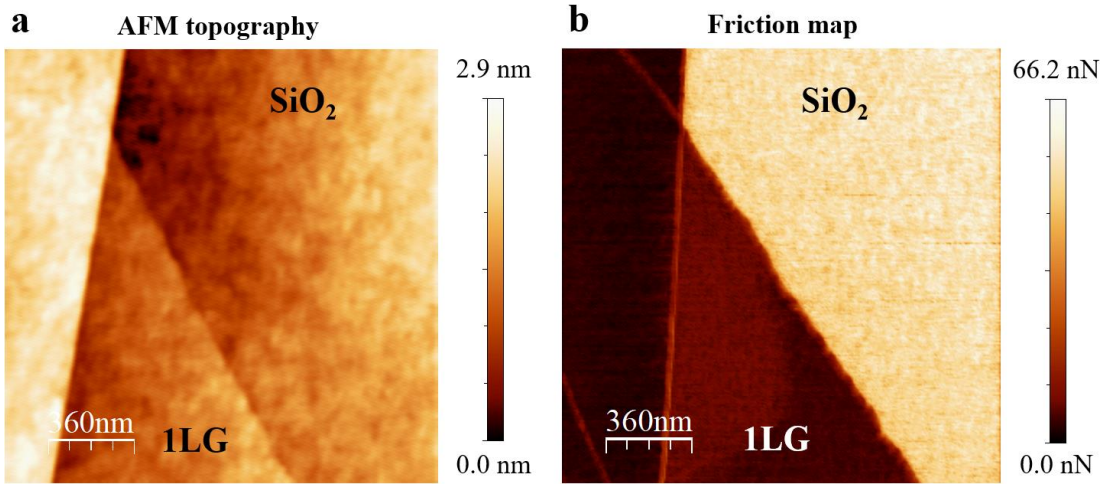

Figure S5. (a) AFM topography and (b) friction force map of ME flake nr. 2, which includes E and SE.

The finite element (FEM) model has been developed in order to reproduce a continuous scan from silica substrate to *2LG* passing through E and SE (Figure S7.a). The substrate and the tip were modeled with solid elements while the graphene flake via shell elements. The thickness of graphene was reduced by a factor 5,[2] i.e t = 0.066 nm (0.34/5 nm), to not overestimate transversal/bending stiffness of the layer. The nominal elastic modulus of graphene (1 TPa) was scaled accordingly in order to keep constant membrane stiffness *Et*. The molecular van der Waals interaction between all the bodies of the model (silica substrate, graphene layers and silicon tip) were implemented via a continuum cohesive zone model based on the Lennard-Jones (LJ) 6-12 potential, as derived and described extensively by Jiang et al.[3] The cohesive normal stress between graphene layers is expressed as derivative of the variational cohesive energy per unit area with respect to the separation distance (perturbation) of the nodes v:

$$\sigma_{\text{cohesive, G/G}} = 8\pi\Psi_{\text{C}}^{2}\varepsilon_{\text{C-C}}s_{\text{C-C}}\left(\frac{s_{\text{C-C}}^{5}}{\left(h_{\text{G/G}}+v\right)^{5}}-\frac{s_{\text{C-C}}^{11}}{\left(h_{\text{G/G}}+v\right)^{11}}\right) \tag{S1}$$

where Ψ is the number of graphene atoms per unit area, $\varepsilon_{\text{C-C}}$ and $s_{\text{C-C}}$ are the LJ potential parameters for carbon-carbon interaction[3], $h_{\text{G/G}} = \sqrt[6]{2s_{\text{C-C}}}$ is the graphene inter-layer equilibrium distance. Note that v corresponds the current node-to-segment separation between contacting interfaces and that the cohesive stress nearly vanishes for $v > 3h_{\text{G/G}}$. On the other hand, the shear stresses associated with van der Waals interaction have been demonstrated to be negligible[3,4], thus we assumed $\tau_{\text{cohesive,G/G}} = 0$. Analogously for the graphene-silica interaction we have:

$$\begin{aligned}\sigma_{\text{cohesive, G/SiO}_2} = {} & 8\pi\Psi_{\text{C}}\,\Psi_{\text{Si}}\,\varepsilon_{\text{C-Si}}s_{\text{C-Si}}\left(\frac{s_{\text{C-Si}}^{5}}{\left(h_{\text{G/SiO}_2}+v\right)^{5}}-\frac{s_{\text{C-Si}}^{11}}{\left(h_{\text{G/SiO}_2}+v\right)^{11}}\right)\\ & + 8\pi\Psi_{\text{C}}\,\Psi_{\text{O}}\,\varepsilon_{\text{C-O}}s_{\text{C-O}}\left(\frac{s_{\text{C-O}}^{5}}{\left(h_{\text{G/SiO}_2}+v\right)^{5}}-\frac{s_{\text{C-O}}^{11}}{\left(h_{\text{G/SiO}_2}+v\right)^{11}}\right)\end{aligned} \tag{S2}$$

with

$$h_{\text{G/SiO}_2} = \left(\frac{\varepsilon_{\text{C-Si}}s_{\text{C-Si}}^{12}+\varepsilon_{\text{C-O}}s_{\text{C-O}}^{12}}{\varepsilon_{\text{C-Si}}s_{\text{C-Si}}^{6}+\varepsilon_{\text{C-O}}s_{\text{C-O}}^{6}}\right)^{1/6} \tag{S3}$$

where the LJ parameters were taken from Kumar *et al.*.[5] For the graphene-Si tip interaction only the first term of Equation (S2) enters into play.

Analogously to MD simulation, the tip was subjected to an imposed F_N and translated in the horizontal plane with a constant velocity towards the E and SE. Rotations of the nodes of the tip were fixed, thus tilt of the simulated AFM is not permitted. Friction force was determined by computing the component of the contact force on the tip ($F_L = F_F$) parallel to scanning motion and the friction coefficient was determined as the slope of the linear fit of the F_F - F_N points.

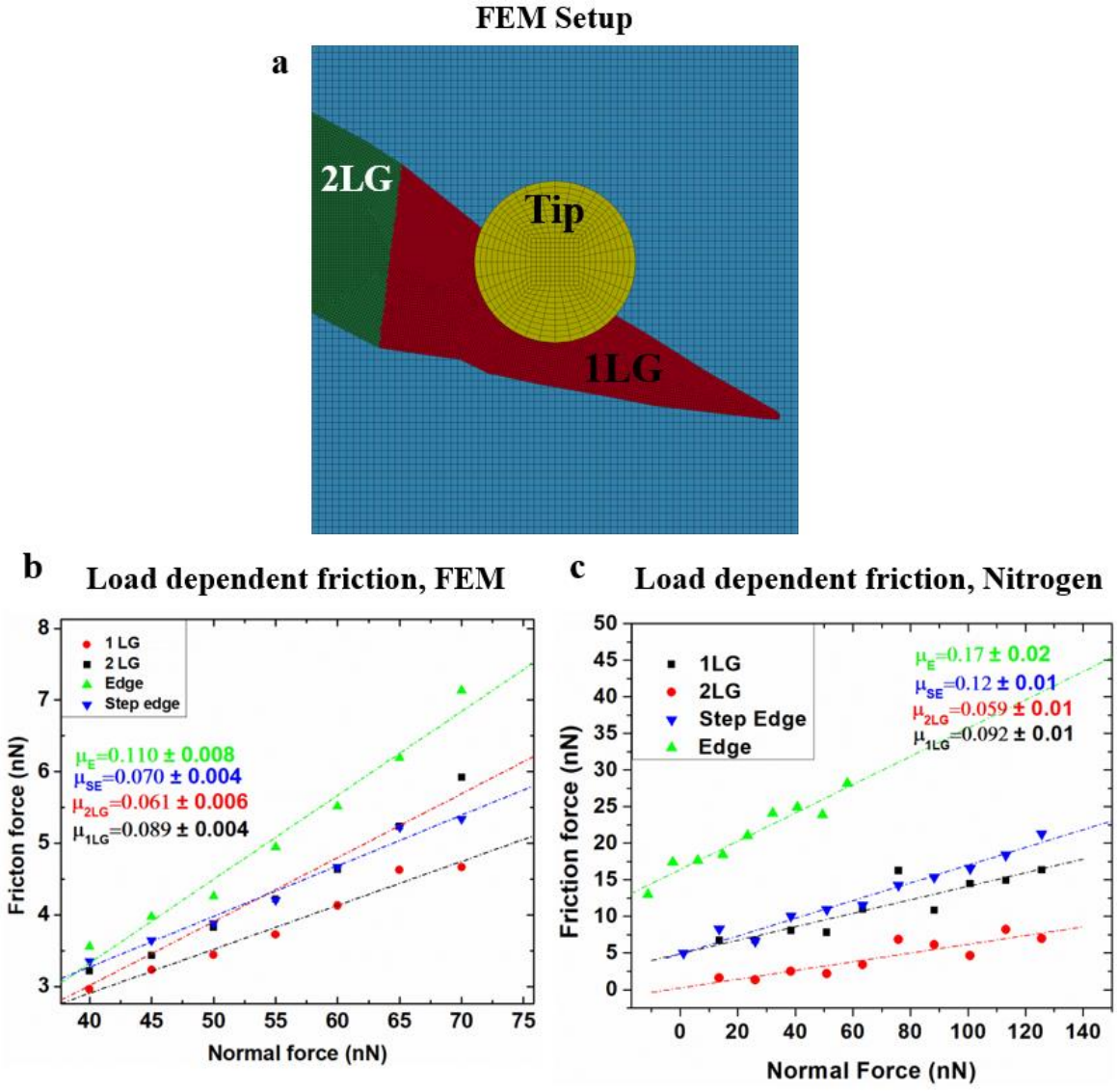

Figure S6. FEM simulation for load dependent friction on 1LG, 2LG and experimental FFM measurement in nitrogen atmosphere. (a) Set-up of finite element method (FEM) of 1LG and 2LG flake against hemispherical silicon slider. (b) FEM based load dependent friction and COF values measured by linear fit for 1LG (~0.089) and 2LG (~ 0.061), SE (~0.07) and E (~0.11). (c) Experimental FFM measurement carried out in nitrogen atmosphere are in close agreement with FEM showing COF values nearly 0.092, 0.059, 0.12, 0.17, respectively.

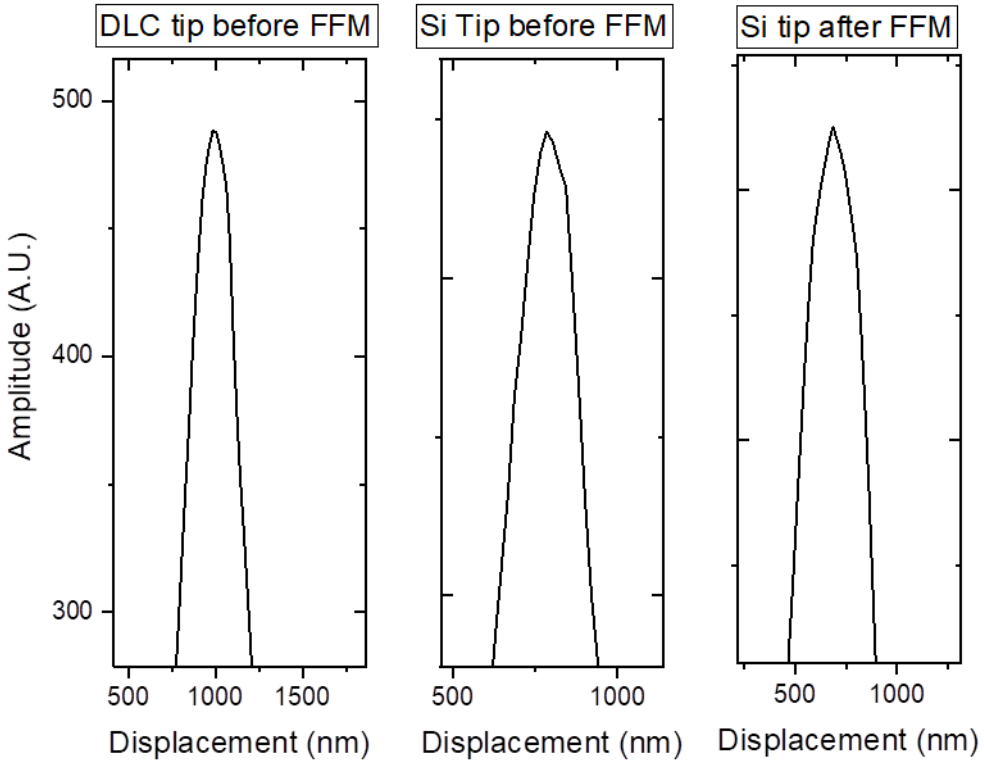

Figure S7. Section profile of different tip apexes scanned over the standard grating. The SEM image DLC tip post FFM measurement is inserted in the main text (Figure 5.k), since grating scanning could remove the graphene flakes around tip apex.

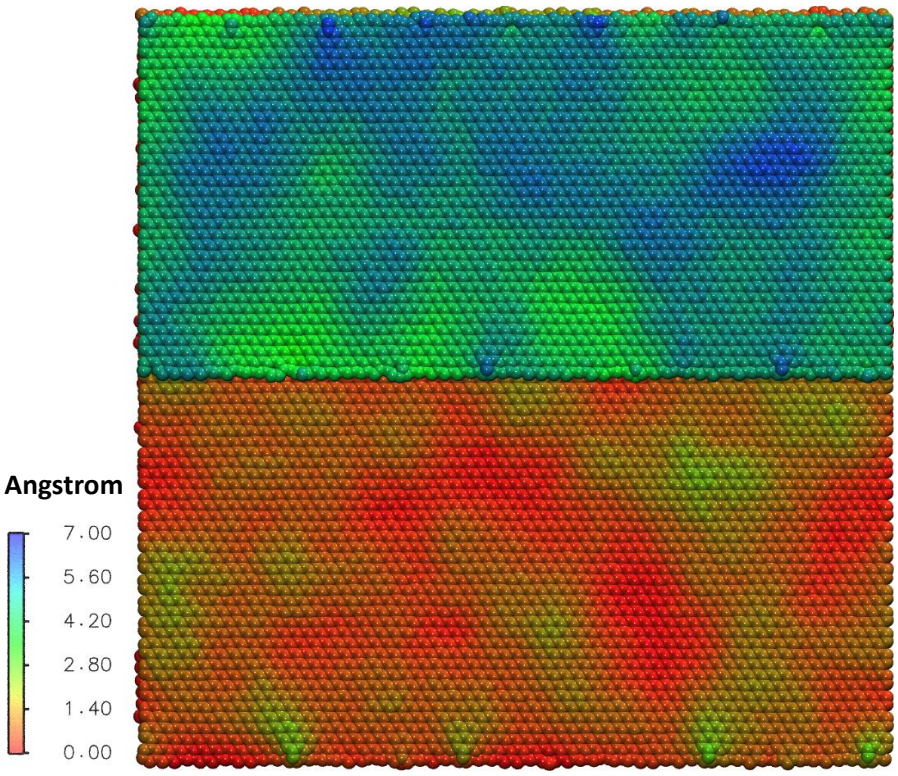

Figure S8. Set-up of MD simulations. Top view of corrugated arrangement of single layer, bi-layer and step-edge atoms. These corrugations were achieved through energy minimization followed by thermalization of the system. The color distribution is associated with the vertical coordinate of carbon atoms of the graphene layers with respect to the substrate reference plane, giving a qualitative sight of the corrugation of the graphene layers.

References

1. Gupta, A.; Chen, G.; Joshi, P.; Tadigadapa, S.; Eklund, P. C. Raman Scattering from High-Frequency Phonons in Supported n-Graphene Layer Films. *Nano Letters* **2006,** *6* (12), 2667-2673.
2. Scarpa, F.; Adhikari, S.; Gil, A.; Remillat, C. The bending of single layer graphene sheets: the lattice versus continuum approach. *Nanotechnology* **2010,** *21* (12), 125702.
3. Jiang, L. Y.; Huang, Y.; Jiang, H.; Ravichandran, G.; Gao, H.; Hwang, K.; Liu, B. A cohesive law for carbon nanotube/polymer interfaces based on the van der Waals force. *Journal of the Mechanics and Physics of Solids* **2006,** *54* (11), 2436-2452.
4. Girifalco, L. A.; M. Hodak, R. S. L. Carbon Nanotubes, Buckyballs, Ropes, and a Universal Graphitic Potential. *Phys. Rev. B* **2000**, *62*, 13104–13110.
5. Kumar S.; Parks D.; Kamrin K. Mechanicistic Origin of the Ultrastrong Adhesion between Graphene and a-SiO2: Beyond van der Waals. *ACS Nano* **2016**, *10* (7) 6552-6562.